

# A Comprehensive Study of Electronic, Optical, and Thermoelectric Characteristics of Cs<sub>2</sub>PbI<sub>2</sub>Br<sub>2</sub> Inorganic Layered Ruddlesden–Popper Mixed Halide Perovskite through Systematic First-Principles Analysis

Souraya Goumri-Said\*

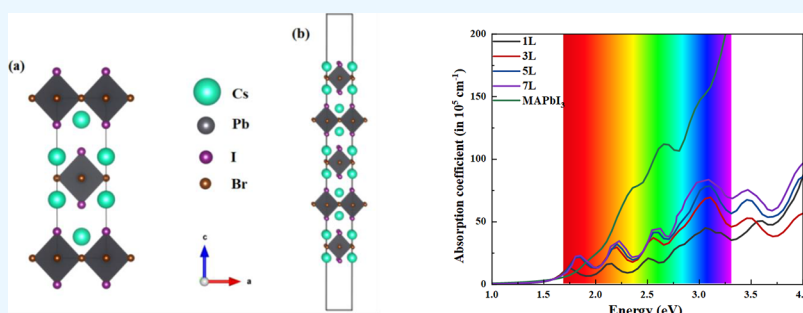
Cite This: *ACS Omega* 2023, 8, 38170–38177

Read Online

ACCESS |

Metrics &amp; More

Article Recommendations



**ABSTRACT:** In this research, we present a comprehensive study on the influence of layer-dependent structural, electronic, and optical properties in the two-dimensional (2D) Ruddlesden–Popper (RP) perovskite Cs<sub>2</sub>PbI<sub>2</sub>Br<sub>2</sub>. Employing first-principles computations within the density functional theory method, including spin orbit coupling contribution, we examine the impact of various factors on the material. Our results demonstrate that the predicted 2D-layered RP perovskite Cs<sub>2</sub>PbI<sub>2</sub>Br<sub>2</sub> structures exhibit remarkable stability both structurally and energetically, making them promising candidates for experimental realization. Furthermore, we observe that the electronic band gap and optical absorption coefficients of Cs<sub>2</sub>PbI<sub>2</sub>Br<sub>2</sub> strongly depend on the thickness variation of the layers. Interestingly, Cs<sub>2</sub>PbI<sub>2</sub>Br<sub>2</sub> exhibits a notable absorption coefficient in the visible region. Using a combination of density functional theory and Boltzmann transport theory, the thermoelectric properties were forecasted. The calculation involved determining the Seebeck coefficient (*S*) and other associated thermoelectric characteristics, such as electronic and thermal conductivities, as they vary with the chemical potential at room temperature. These findings open up exciting opportunities for the application of this 2D RP perovskite in solar cells and thermoelectric devices, owing to its unique properties.

## 1. INTRODUCTION

Inorganic halide-based perovskites have remarkable structural properties and also have a lot of potential for use in a variety of energetic applications, such as photovoltaics, ionizing radiation detectors, and light-emitting diodes (LEDs).<sup>1–5</sup> However, inorganic perovskite materials with three-dimensional (3D) bulk configurations are unstable, and the black active phase eventually transforms into a yellow nonperovskite polymorph structure.<sup>6</sup> Two-dimensional (2D) perovskites, referred to as Ruddlesden–Popper (RP) perovskites, exhibit greater stability in environmental and improved optoelectronic features when compared to their 3D perovskite counterparts.<sup>7,8</sup> They have emerged as one of the most attractive research subjects because of the enormous potential of their application in solar cell technology and light emitters.<sup>9,10</sup> The typical chemical structure of 2D Ruddlesden–Popper perovskites is defined as A<sub>*n*+1</sub>B<sub>*n*</sub>X<sub>3*n*+1</sub> (*n* = 1, 2, ...), where A is a large cation, Cs, B is a metal cation, Pb,

X represents a halogen atom (I, Br), and *n* specifies the number of layers ([BX<sub>6</sub>]<sup>4–</sup> octahedral layers).<sup>10</sup>

For the past decade, a significant amount of theoretical and experimental work on the optical and electronic characteristics of hybrid layered RP perovskites has been described. For example, Tsai et al.<sup>11</sup> produced hybrid layered RP perovskite (BA)<sub>2</sub>(MA)<sub>*n*–1</sub>Pb<sub>*n*</sub>I<sub>3*n*+1</sub> with a cell efficiency of 12.52%. They revealed that the device structures had better stability than that of comparable 3D perovskite. Zheng et al.<sup>12</sup> reported that the carrier transport rates of 2D RP perovskite were considerably

Received: June 17, 2023

Accepted: September 21, 2023

Published: October 3, 2023



increased by narrowing the space between the cations. Zhao et al.<sup>13</sup> examined the electronic band gap, energies of exciton binding, and optical absorption feature in the hybrid 2D layered perovskite (PEA)<sub>2</sub>PbI<sub>4</sub>, by indicating a potential optoelectronic application. Abid et al.<sup>14</sup> reported a combined study of spectroscopic ellipsometry thin film and theoretical calculations of optoelectronic of [(C<sub>9</sub>H<sub>19</sub>NH<sub>3</sub>)<sub>2</sub>PbI<sub>2</sub>Br<sub>2</sub>] 2D perovskite. Recently, Li et al.<sup>15</sup> revealed that a hybrid 2D layered perovskite (BA)<sub>2</sub>(MA)<sub>3</sub>Pb<sub>4</sub>I<sub>13</sub> solar cell had an efficiency of about 15%. In recent research, Dong et al.<sup>16</sup> obtained a device efficiency of 16.72% for (ThFA)<sub>2</sub>MA<sub>n-1</sub>Pb<sub>n</sub>I<sub>3n+1</sub> ( $n = 3$ ) solar cells based on the RP structure. Additionally, Xi et al. achieved a 2D hybrid solar cell efficiency of 14.76%.<sup>17</sup> However, inorganic 2D RP perovskites have garnered far less interest than hybrid 2D perovskites due to the challenge of their experimental synthesis. In comparison to hybrid materials, the pure inorganic RP structures of halide perovskites are predicted to be more robust under extreme circumstances. Recently, Li et al.<sup>18</sup> reported a design, fabrication, and experimental characterization of 2D Cs<sub>2</sub>PbI<sub>2</sub>Cl<sub>2</sub> and Cs<sub>2</sub>SnI<sub>2</sub>Cl<sub>2</sub> in which the 2D RP mixed halide perovskite exhibits excellent thermal and environmental stability, revealing prospective prospects for application in detection and other optoelectronic components. In this manner, the optical and electronic characteristics of all-inorganic 2D RP perovskites have steadily gained interest. Through the use of first-principles computations, Pan et al.<sup>19</sup> examined the optoelectronic characteristics of the 2D RP perovskite Cs<sub>2</sub>PbI<sub>2</sub>Cl<sub>2</sub>. Moreover, Xu et al.<sup>20</sup> calculated the electron and hole charge carrier mobilities of 2D RP inorganic perovskite by variation of layers. More recently, Saffari et al.<sup>21</sup> investigated thorough theoretical analysis of the 2D RP inorganic perovskite as well as single junction solar cells and tandem cells. The prospective applications of RP-phase halide perovskites are however limited by poor photoelectric characteristics, notably, a large bandgap (up to 3.04 eV for Cs<sub>2</sub>PbI<sub>2</sub>Cl<sub>2</sub>).<sup>18</sup> Therefore, it is necessary to enhance the electronic performance and optical properties of all-inorganic 2D RP perovskites by proposing to replace a Cl atom with a Br atom.

First-principles computations are used in this study to thoroughly evaluate the structural, electronic, and optical absorption properties of the all-inorganic, 2D-layered RP perovskite Cs<sub>2</sub>PbI<sub>2</sub>Br<sub>2</sub> with various layers. In particular, we investigated the optical absorption coefficients and band structures of the 2D-layered RP perovskite Cs<sub>2</sub>PbI<sub>2</sub>Br<sub>2</sub>. In order to weigh the advantages and disadvantages, we also contrasted the optical absorption coefficient of the predicted 2D RP perovskite Cs<sub>2</sub>PbI<sub>2</sub>Br<sub>2</sub> with those of the MAPbI<sub>3</sub> substance. In addition, we solved the Boltzmann transport equations in order to evaluate the thermoelectric performance of Cs<sub>2</sub>PbI<sub>2</sub>Br<sub>2</sub>. This comparison may offer theoretical support for the creation of 2D-layered, entirely inorganic perovskites for photovoltaic applications.

## 2. COMPUTATIONAL DETAILS

Theoretical computations are performed through the calculation software QuantumATK.<sup>22</sup> The exchange-correlation function of the electrons is evaluated using the generalized gradient approximation (GGA) functional developed by Perdew–Burke–Ernzerhof (PBE).<sup>23</sup> The pseudoDojo pseudo-potential<sup>24</sup> and the linear combination of atomic orbitals (LCAO) basis set were employed. All geometry structures are totally relaxed by using the limited-memory Broyden–Fletcher–Goldfarb–Shanno (LBFGS) optimizer. The con-

vergence requirements for force and energy during optimization are set at 0.03 eV/Å and 10<sup>-5</sup> eV, respectively. A 5 × 5 × 2 Monkhorst Pack<sup>25</sup> set of k-points is used to sample the Brillouin zone with a density mesh cutoff value of 230 Ry. DFT-D2 method of Grimme<sup>26</sup> is used to incorporate long-range van der Waals dispersion correction. All the electronic and optical properties were computed by using PBE including the spin orbit coupling (SOC) and the Heyd–Scuseria–Ernzerhof hybrid (HSE06) functional<sup>27–29</sup> plus SOC contribution.<sup>30</sup>

## 3. RESULTS AND DISCUSSION

The bulk structure of Cs<sub>2</sub>PbI<sub>2</sub>Br<sub>2</sub> follows the K2NiF<sub>4</sub>-type structure and belongs to the tetragonal space group of *I4/mmm* (no. 139) with the lattice parameters of  $a = b = 5.6385$  Å,  $c = 18.879$  Å in which the lead atom is located in the core of octahedron, and the corners are occupied by I and Br atoms where the out-of-plane terminal site is occupied by I atoms and the in-plane bridging site by Br atoms. The Cs cation serves as the spacer, balancing charge. A single and multilayered 2D RP perovskite Cs<sub>2</sub>PbI<sub>2</sub>Br<sub>2</sub> was modeled from the optimized bulk structure by adopting a vacuum spacing of 15 Å along the *c*-direction to eliminate the interaction between periodic adjacent structures. We classified the bilateral inorganic cations Cs and the octahedra [PbI<sub>2</sub>Br<sub>4</sub>]<sup>4-</sup> as one layer to preserve the dimensional RP structure as shown in Figure 1. The predicted

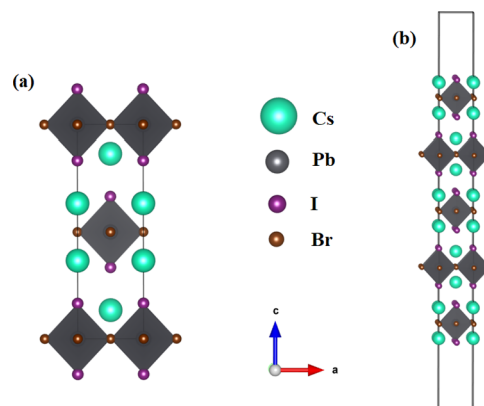


**Figure 1.** Schematics of the crystal structures of (a) bulk Cs<sub>2</sub>PbI<sub>2</sub>Br<sub>2</sub> and (b) 2D five-layered RP perovskite Cs<sub>2</sub>PbI<sub>2</sub>Br<sub>2</sub> (Cs in cyan, Pb in gray, I in purple, and Br in brown).

lattice parameters and bond lengths of 2D-layered RP perovskite Cs<sub>2</sub>PbI<sub>2</sub>Br<sub>2</sub> with one layer, three layers, five layers, and seven layers are summarized in Table 1. We noticed that the calculated equilibrium parameters steadily increase as the number of layers rises from single to seven layers, and they consistently preserve the equality of the relationships between the lattice parameters *a* and *b* under structural optimization. This differs from that found

**Table 1.** 2D-Layered RP Perovskite Cs<sub>2</sub>PbI<sub>2</sub>Br<sub>2</sub>'s Optimal Lattice Parameters, Bond Lengths, and Energy during Crystallization for the First, Third, and Fifth Layers

	<i>a</i> (Å)	<i>b</i> (Å)	<i>c</i> (Å)	Pb–I (Å)	Pb–Br (Å)	<i>E<sub>f</sub></i>
bulk	5.984	5.984	19.505	3.230	3.000	−9.909
1L	5.870	5.870	29.449	3.232	2.935	−9.450
3L	5.930	5.930	48.917	3.222	2.975	−9.807
5L	5.931	5.931	68.241	3.238	2.965	−9.879
7L	5.932	5.932	87.650	3.226	2.966	−9.909

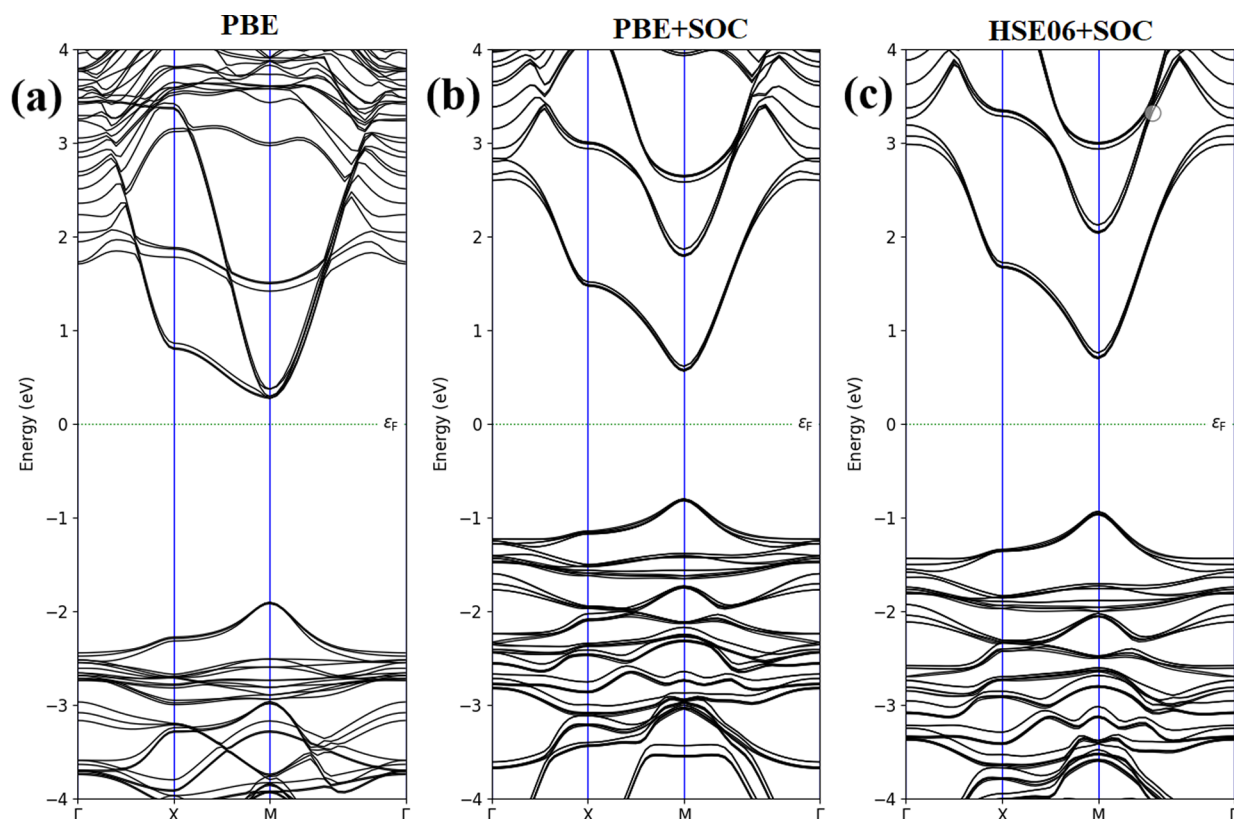


**Figure 2.** Calculated band structures of 2D RP perovskite  $\text{Cs}_2\text{PbI}_2\text{Br}_2$  using the (a) PBE, (b) PBE + SOC, and (c) HSE06 + SOC levels of approximation.

in hybrid organic–inorganic 2D RP perovskites ( $a \neq b$ ) that include tilting octahedra.<sup>11,31</sup> To gain information on the energetic stability of 2D RP  $\text{Cs}_2\text{PbI}_2\text{Br}_2$ , we calculated the energy of formation ( $E_f$ ) using the following equations  $E_f = E_{\text{Cs}_2\text{PbI}_2\text{Br}_2} - 2E_{\text{CsBr}} - E_{\text{PbI}_2}$ , where,  $E_{\text{Cs}_2\text{PbI}_2\text{Br}_2}$ ,  $E_{\text{CsBr}}$ , and  $E_{\text{PbI}_2}$  represent the corresponding total energies. The calculated formation energies for single and multilayers of  $\text{Cs}_2\text{PbI}_2\text{Br}_2$  are listed in Table 1. The negative formation energy indicates that they are energetically stable. Moreover, the Goldschmidt tolerance factor can be applied to evaluate the stability of the structure of 2D RP perovskites.<sup>32,33</sup> The appropriate tolerance factor range for perovskite structures is 0.7–1.1.<sup>34</sup> The estimated tolerance factor for  $\text{Cs}_2\text{PbI}_2\text{Br}_2$  material is 0.931, which exhibits a rational structure by satisfying the ideal tolerance factor.

The calculated electronic band structures of three layers RP halide perovskite  $\text{Cs}_2\text{PbI}_2\text{Br}_2$  are shown in Figure 2 using PBE and HSE06 schemes of approximation by including the SOC contribution. All inorganic perovskite structures are direct band gap semiconductors, whereas both the top of the valence band (VB) and the bottom of the conduction band (CB) are situated at the M point. We found that the band structure configurations for the HSE06 and PBE levels are similar, but as expected, the PBE technique underestimates the value of the band gap for perovskite systems. It is shown that the predicted band gap value obtained with HSE06 functional of bulk  $\text{Cs}_2\text{PbI}_2\text{Br}_2$  is found to be 1.72 eV, which is smaller than that of bulk  $\text{Cs}_2\text{PbI}_2\text{Cl}_2$  (3.04 eV).<sup>18,35</sup> The values of the bandgap at different levels of approximations for the single, three, five, and seven 2D layered RP perovskites are gathered in Table 2. It is found from Table 2 that there is a decrease of 0.13 eV in the bandgap from the bulk structure to a single layer. It is important to highlight that our

**Table 2.** Computed Band Gap for All-Inorganic 2D Layered RP Perovskite  $\text{Cs}_2\text{PbI}_2\text{Br}_2$  with Various Thicknesses by PBE, PBE + SOC, HSE06, and HSE06 + SOC

	PBE	PBE + SOC	HSE	HSE + SOC
bulk	2.22	1.43	2.59	1.72
1L	2.13	1.32	2.49	1.59
3L	2.18	1.36	2.53	1.63
5L	2.18	1.37	2.53	1.64
7L	2.18	1.38	2.55	1.66

findings support those of the previous theoretical studies.<sup>36,37</sup> They additionally noticed a little rise in the bandgap from the bulk to 2D structures. We reported the band structures of the 2D RP perovskite system using the PBE+SOC approach, as shown in Figure 2b, to account for the relativistic impacts in the heavy Pb atoms. Comparing PBE+SOC to PBE, the band gap is significantly smaller based on the band structure plot in Figure 2a,b. It is observed that, by adopting SOC, the maximum of VB shifts toward a higher energy level but the minimum of CB is little changed and thus leads to the decrease in the band gap. In comparison to those computed just by PBE, the band edges estimated by PBE + SOC illustrated in Figure 2b appear substantially steeper. The PBE and PBE + SOC approaches, however, are unable to provide precise band gaps. In order to fairly adjust the band gaps, we computed the band structure using the HSE06 functional with the SOC contribution. PBE + SOC calculations of three-layer 2D RP perovskite result in band structures that are just the same as those produced by HSE06 + SOC calculations. It is also noticed that the values of bandgaps slightly change with the increase of layers; it could be because the equilibrium parameters and bond lengths have hardly

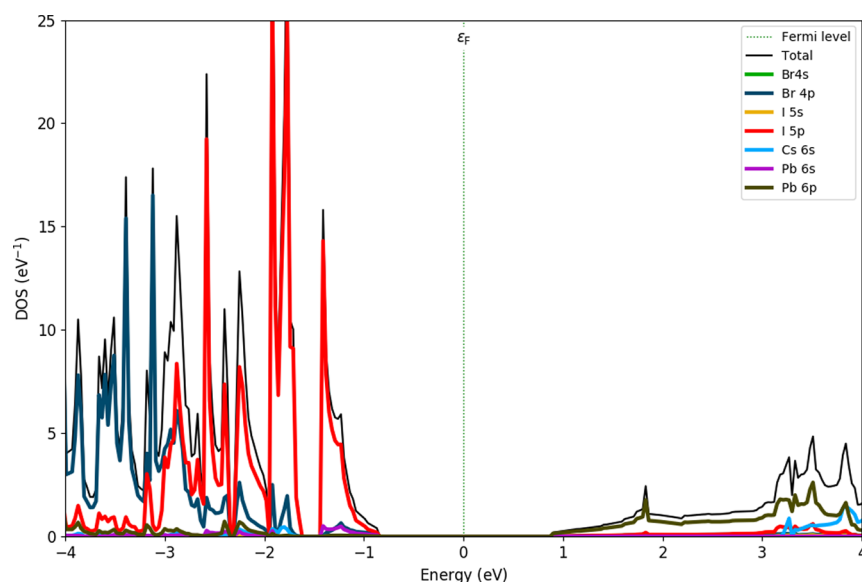


**Figure 3.** Total and partial PDOS using the HSE06 + SOC method for 2D RP perovskite  $\text{Cs}_2\text{PbI}_2\text{Br}_2$ .

altered. The projected density of states (PDOS) is calculated and evaluated to indicate the contribution of each component to the estimated band structure, as shown in Figure 3. From PDOS analysis, the upper edge of the VB is mostly contributed by I 5p states and little smaller contribution of Br 4p and Pb 6s states, whereas the lower edge of the CB is mainly composed of Pb 6p states and much lower contribution of I 5p and Br 4p states. The Cs cations are present in the deeper region as compared to the top of the VB and bottom of the CB.

The real and imaginary components of the frequency-dependent dielectric constant are used to calculate the optical absorption spectra of 2D layered RP  $\text{Cs}_2\text{PbI}_2\text{Br}_2$  to determine how much light can be absorbed. The average absorption coefficients of bulk and 2D RP  $\text{Cs}_2\text{PbI}_2\text{Br}_2$  are shown in Figure 4 and are compared to  $\text{MAPbI}_3$ . The range of visible light (1.62–3.11 eV) is pointed out during analysis. It exhibits good optical absorption characteristics in the visible range. The first absorption peak of  $\text{MAPbI}_3$  is found at energies of 2.36 eV,

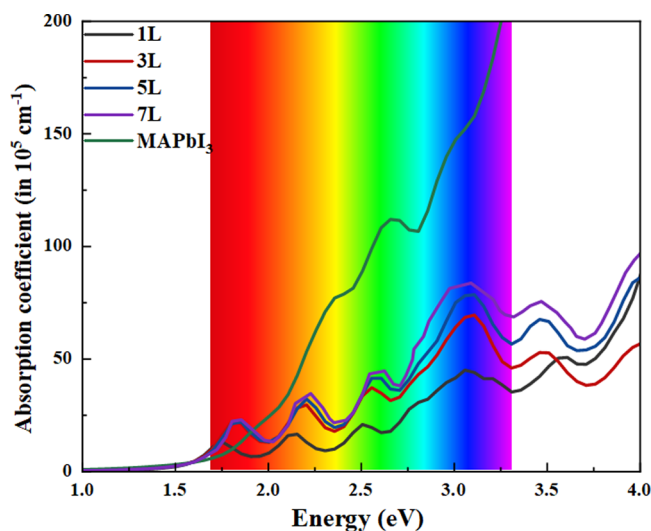


**Figure 4.** Calculated absorption spectra of 2D RP perovskite  $\text{Cs}_2\text{PbI}_2\text{Br}_2$  with different thicknesses obtained by HSE06 + SOC compared with bulk  $\text{MAPbI}_3$ .

while they appear at energies of 1.74, and 1.8305 eV for single, and multilayers RP  $\text{Cs}_2\text{PbI}_2\text{Br}_2$ . We observe greater absorption for 2D RP  $\text{Cs}_2\text{PbI}_2\text{Br}_2$  than for  $\text{MAPbI}_3$  in the high-energy region of 1.70–2.0 eV. However,  $\text{MAPbI}_3$  exhibits the highest absorption in the low-energy range (2.0–3.11 eV) and ultraviolet.<sup>38,39</sup> On the whole, the light absorption capability of 2D layered RP perovskites shows little variation in the visible spectrum and slightly rises with an increase in the layer thickness at about 3.0 eV. In addition, the absorption at about 2.6 eV gradually shifts to the higher photon energy with an increase in thickness. These blue-shifts of the absorption could be caused by the increase of bandgaps in 2D layered RP perovskite  $\text{Cs}_2\text{PbI}_2\text{Br}_2$  with the increase of thickness.

Finally, transport properties of the 2D perovskite have been investigated employing Boltzmann transport theory, the constant relaxation time approaches, and the theoretical band structures. When the Boltzmann transport theory and the constant relaxation time approximation are applied to study thermoelectric properties, several key quantities can be calculated. Here are the main thermoelectric properties obtained from these approaches:<sup>40–42</sup>

**Seebeck coefficient (thermopower):** The Seebeck coefficient, denoted as  $S$ , is a measure of the electric voltage generated in response to a temperature gradient. It quantifies the ability of a material to convert a temperature difference to an electrical voltage. In Boltzmann transport theory, the Seebeck coefficient is calculated as the ratio of the electrical conductivity ( $\sigma$ ) to the electronic thermal conductivity ( $\kappa_e$ ) multiplied by the temperature gradient ( $\nabla T$ ):

$$S = - (1/eT) \times (\sigma/\kappa_e) \times \nabla T$$

where  $e$  is the electronic charge and  $T$  is the temperature.

The electrical conductivity, denoted as  $\sigma$ , characterizes the ability of a material to conduct an electric current. In the constant relaxation time approximation, the electrical conductivity can be calculated using the relaxation time ( $\tau$ ) and the charge carrier concentration ( $n$ ):

$$\sigma = e^2 \times n \times \tau \times \mu$$

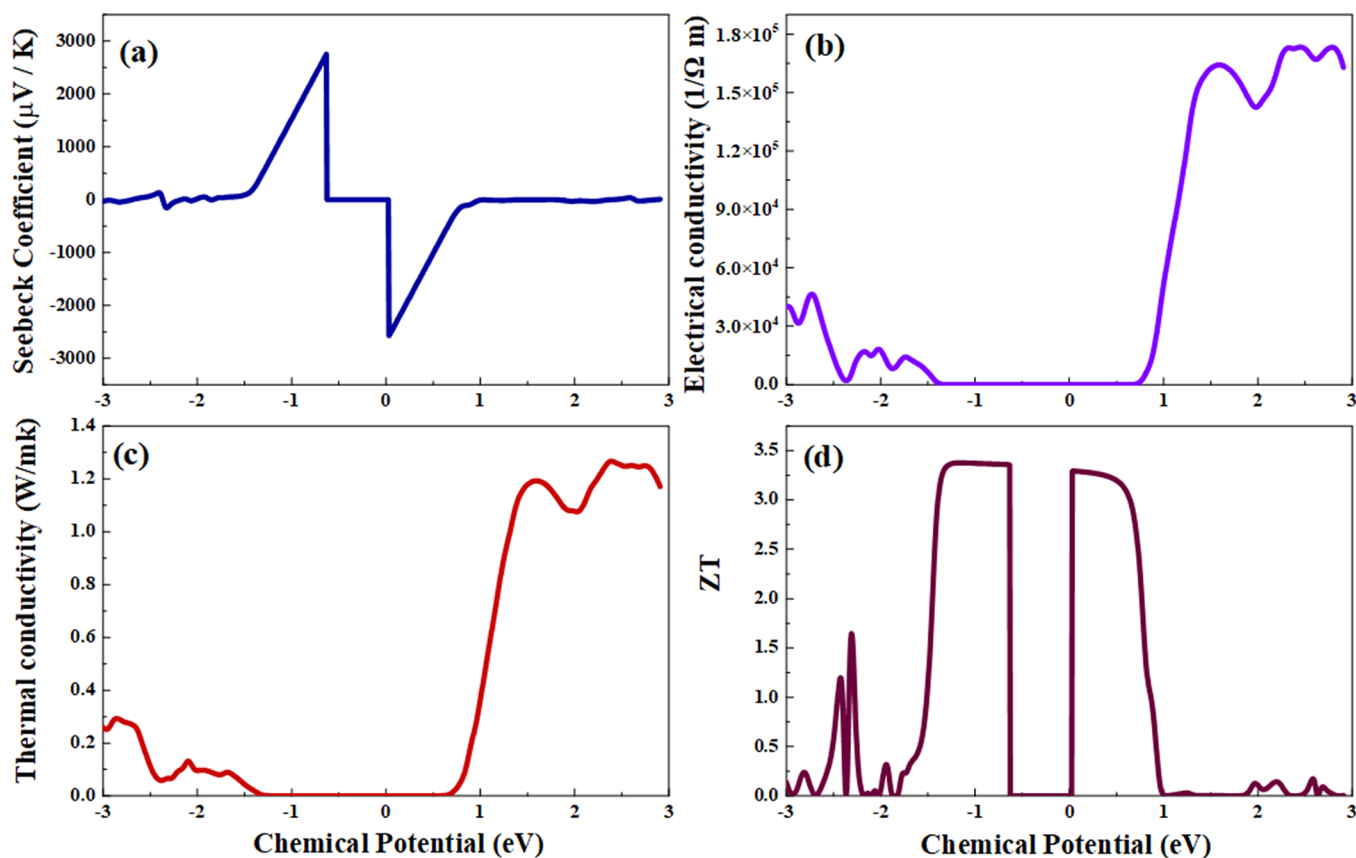


**Figure 5.** Calculated transport coefficients of  $\text{Cs}_2\text{PbI}_2\text{Br}_2$  as a function of chemical potential ( $\mu$ ): (a) Seebeck coefficient, (b) electrical conductivity, (c) thermal conductivity, and (d) figure of merit.

where  $e$  is the electronic charge and  $\mu$  is the charge carrier mobility.

**Electronic thermal conductivity:** The electronic thermal conductivity, denoted as  $\kappa_e$ , represents the ability of charge carriers (electrons or holes) to transport thermal energy. It is related to the charge carrier concentration ( $n$ ), relaxation time ( $\tau$ ), and charge carrier mobility ( $\mu$ ) in the constant relaxation time approximation:

$$\kappa_e = (1/3) \times (e^2 \times n \times \tau) \times \mu \times v^2$$

where  $v$  is the Fermi velocity.

**Power factor:** The power factor (PF) is a figure of merit (ZT) used to evaluate the thermoelectric efficiency of a material. It is defined as the product of the square of the Seebeck coefficient ( $S^2$ ) and the electrical conductivity ( $\sigma$ ):  $\text{PF} = S^2 \sigma$ . In Figure 5, we report all pertinent TE properties as defined above.

The performance of the TE apparatus can be determined by the dimensionless figure of merit ZTe given by  $ZTe = \frac{S^2 \sigma}{K}$

According to rigid band approximations (RBA), just the chemical potential changes from the innate limit depending on the doping type, but the band structure is unchanged. A higher Seebeck coefficient for effective TE materials is important. The Seebeck coefficient is positive (negative) for moderate  $p$ -type ( $n$ -type) materials. For  $n$ -( $p$ ) type doping, the chemical potential is positive (negative). The upper side of Figure 5 in the range of  $-3$  to  $3$  eV shows the variation of the Seebeck coefficient at room temperature. To decrease the Joule heating effect, the compound must have higher electrical conductivity for efficient thermoelectric devices. For  $n$ -type doping, the chemical

potential ( $\mu$ ) moves in the CB. However, for  $p$ -type doping,  $\mu$  moves down in the VB.  $N$ -type materials, larger and more negative  $S$  values are obtained away from the band edges. It can be seen that from  $-1.5$  to  $-0.61$  eV of the chemical potential ( $\mu$ ), the Seebeck coefficient has maximum peaks indicating that the 2D perovskite compound exhibits good thermoelectric properties for these points, while beyond these points,  $S$  is zero. The electrical conductivity ( $\sigma$ ) is the other crucial parameter that provides an efficient thermoelectric figure of merit (ZT).  $\sigma$  is an intrinsic property of any material for all compounds as shown in the above Figure 5b. We found that there is a significant change in  $\sigma$  with chemical potential ( $\mu$ ) showing asymmetrical behavior (between  $p$ - and  $n$ -type zones) where  $\sigma$  is found to be zero between  $-1.34$  and  $0.72$  eV and then it starts to increase to higher values in the  $n$ -type region. Using the same constant relaxation time assumption as before, we computed the thermal conductivity ( $\kappa_e$ ) at a temperature of 300 K as a function of the chemical potential ( $\mu$ ). The outcome is displayed in Figure 5c. Minimum values of  $\kappa_e$  are seen in the chemical potential ranges between  $-3$  and  $+3$  eV, which are present in the regions where the tested materials can operate with the greatest efficiency. We discover that 2D perovskite exhibits the highest, which is around  $0.28$  W/mK at  $-2.8$  eV for  $p$ -type. However, at  $2.39$  eV and  $1.27$  W/mK,  $\kappa_e$  achieves its maximum in the  $n$ -type region. Effective and dependable thermoelectrics are made from materials with low thermal conductivity.<sup>43–45</sup> The thermal conductivity occurs by vibrations of the electrons and lattice. For efficient thermoelectric devices, there should be low values of the value of thermal conductivity. We have deduced the ZT (figure of merit) from the former transport properties versus the

chemical potential. It is well-known that for an efficient thermoelectric device, the ZT parameter should be bigger than or equal to 1. In our case, we were able to find ZT higher than 1 in p- and n-types zones mainly for  $\mu = -2.45$  to 1 eV with zero values  $-0.63$  to 0.018 eV. We can relate the behavior of the 2D perovskites to some examples such as reported for graphene. While pristine graphene has limited thermoelectric performance, modifications such as introducing defects, functionalizing with dopants, or creating heterostructures have shown promise in enhancing its ZT value. For instance, graphene nanoribbons with edge disorder or graphene-based heterostructures incorporating other materials like boron nitride have demonstrated improved thermoelectric properties.<sup>46–48</sup> Also, transition metal dichalcogenides (TMDs), such as MoS<sub>2</sub> and WSe<sub>2</sub>, are a class of 2D materials with unique electronic and thermal properties. TMDs exhibit an intrinsic thickness-dependent bandgap, making them suitable for thermoelectric applications. By manipulating the layer thickness or introducing defects, researchers have achieved an enhanced thermoelectric performance in TMDs. For example, few-layer MoS<sub>2</sub> with sulfur vacancies has shown improved thermoelectric properties, including high Seebeck coefficients and reduced thermal conductivity.<sup>49–51</sup> Furthermore, black phosphorus (BP) is described as a layered material with a puckered structure. It possesses anisotropic thermal and electrical conductivities, which can be advantageous for thermoelectric applications. The presence of multiple valleys in the electronic band structure of BP allows for enhanced Seebeck coefficients. Additionally, the doping and nanostructuring of BP have been explored to enhance its thermoelectric performance. BP-based nanocomposites and heterostructures have shown potential for achieving high ZT values.<sup>52–54</sup> It is worth noting that while advancements have been made, there are still challenges to overcome, such as scalability, stability, and manufacturing techniques, before these materials can be effectively integrated into practical thermoelectric devices. Nonetheless, the exploration of 2D materials for thermoelectric applications provides exciting avenues for efficient energy conversion and offers possibilities for future technological advancements.

#### 4. CONCLUSIONS

A 2D-layered RP perovskite Cs<sub>2</sub>PbI<sub>2</sub>Br<sub>2</sub> was modeled, with increasing layers resulting in larger lattice parameters. The formation energy calculations indicate that the perovskites are energetically stable. The Goldschmidt tolerance factor for Cs<sub>2</sub>PbI<sub>2</sub>Br<sub>2</sub> falls within the appropriate range, indicating structural stability. The electronic band structures of Cs<sub>2</sub>PbI<sub>2</sub>Br<sub>2</sub> were calculated by using different approximation schemes. The bulk and layered perovskite structures were found to be direct band gap semiconductors. The band structure configurations were similar between the approximation schemes, but the PBE technique underestimated the band gap. The band gap slightly increased from bulk to a single layer and decreased with increasing layers. Incorporating relativistic effects shifted the maximum of VB to higher energy levels and decreased the band gap. The HSE06 functional with SOC provided more accurate band gap values. The projected density of states analysis revealed the contributions of different atomic components to the valence and conduction bands. The Cs cations were located deeper within the structure compared to the band edge. Optical absorption spectra of bulk and 2D RP Cs<sub>2</sub>PbI<sub>2</sub>Br<sub>2</sub> show good visible light absorption. Cs<sub>2</sub>PbI<sub>2</sub>Br<sub>2</sub> exhibits higher absorption at high energies, while MAPbI<sub>3</sub> dominates in the low-energy and

ultraviolet ranges. The dimensionless figure of merit ZT determines the performance of the TE apparatus. The Seebeck coefficient, electrical conductivity, and thermal conductivity were analyzed for 2D perovskite compounds. The materials exhibited good thermoelectric properties in specific chemical potential ranges. Similar behavior was observed in graphene and transition metal dichalcogenides. Challenges in scalability, stability, and manufacturing techniques remain for practical implementation.

#### AUTHOR INFORMATION

##### Corresponding Author

Souraya Goumri-Said – Department of Physics, College of Science and General studies, Alfaisal University, Riyadh 11533, Saudi Arabia; [orcid.org/0000-0002-9333-7862](https://orcid.org/0000-0002-9333-7862); Email: [sosaid@alfaisal.edu](mailto:sosaid@alfaisal.edu)

Complete contact information is available at:  
<https://pubs.acs.org/10.1021/acsomega.3c04323>

##### Notes

The author declares no competing financial interest.

#### ACKNOWLEDGMENTS

S.G.-S. thanks the office of research at Alfaisal University in Saudi Arabia for supporting this research work through internal project (IRG) number 22413.

#### REFERENCES

- (1) Kumawat, N. K.; Liu, X.-K.; Kabra, D.; Gao, F. Blue perovskite light-emitting diodes: progress, challenges and future directions. *Nanoscale* **2019**, *11*, 2109.
- (2) Stranks, S. D.; Nayak, P. K.; Zhang, W.; Stergiopoulos, T.; Snaith, H. J. Formation of thin films of organic-inorganic perovskites for high-efficiency solar cells. *Angew. Chem., Int. Ed.* **2015**, *54*, 3240.
- (3) Yang, T.; Li, F.; Zheng, R. Recent advances in radiation detection technologies enabled by metal-halide perovskites. *Mater. Adv.* **2021**, *2*, 6744.
- (4) Xiang, W.; Liu, S.; Tress, W. A review on the stability of inorganic metal halide perovskites: challenges and opportunities for stable solar cells. *Energy Environ. Sci.* **2021**, *14*, 2090–2113.
- (5) Nie, T.; Fang, Z.; Ren, X.; et al. Recent Advances in Wide-Bandgap Organic–Inorganic Halide Perovskite Solar Cells and Tandem Application. *Nano-Micro Lett.* **2023**, *15*, 70 DOI: [10.1007/s40820-023-01040-6](https://doi.org/10.1007/s40820-023-01040-6).
- (6) Breniaux, E.; Dufour, P.; Karthick, S.; Yildirim, C.; Bouclé, J.; Vedraïne, S.; Ratel-Ramond, N.; Tenaillé, C. Perovskite CsPbI<sub>2</sub>Br Thin Films Prepared under Nitrogen Flow and Black Phase Stabilization in the Presence of a Two-Dimensional Inorganic Halide Material and Indium. *Eur. J. Inorg. Chem.* **2022**, *2022*, No. e202200490.
- (7) Cheng, P.; Xu, Z.; Li, J.; Liu, Y.; Fan, Y.; Yu, L.; Smilgies, D. E.; Müller, C.; Zhao, K.; Liu, S. F. Ligand-Size Related Dimensionality Control in Metal Halide Perovskites. *ACS Energy Lett.* **2018**, *3*, 1975–1982.
- (8) Fu, W.; Wang, J.; Zuo, L.; Gao, K.; Liu, F.; Ginger, D. S.; Jen, A. K. Y. Two-Dimensional Perovskite Solar Cells with 14.1% Power Conversion Efficiency and 0.68% External Radiative Efficiency. *ACS Energy Lett.* **2018**, *3*, 2086–2093.
- (9) (a) Chen, X.; Ding, M.; Luo, T.; Ye, T.; Zhao, C.; Zhao, Y.; Zhang, W.; Chang, H. Self-assembly of 2D/3D perovskites by crystal engineering for efficient air-processed, air-stable inverted planar perovskite solar cells. *ACS Appl. Energy Mater.* **2020**, *3*, 2975–2982. (b) Kong, L.; Zhang, X.; Li, Y.; Wang, H.; Jiang, Y.; Wang, S.; You, M.; Zhang, C.; Zhang, T.; Kershaw, S. V.; et al. Smoothing the energy transfer pathway in quasi-2D perovskite films using methanesulfonate leads to highly efficient light-emitting devices. *Nat. Commun.* **2021**, *12*, 1246.

- (10) Lu, J.; Zhou, C.; Chen, W.; Wang, X.; Jia, B.; Wen, X. Origin and physical effects of edge states in two-dimensional Ruddlesden-Popper perovskites. *iScience* **2022**, *25*, No. 104420.
- (11) Tsai, H.; Nie, W.; Blancon, J.-C.; Stoumpos, C. C.; Asadpour, R.; Harutyunyan, B.; Verduzco, R.; Crochet, J.; Tretiak, S.; Pedesseau, L.; et al. High-Efficiency Two-Dimensional Ruddlesden-Popper Perovskite Solar Cells. *Nature* **2016**, *536*, 312.
- (12) Zheng, K.; Chen, Y.; Sun, Y.; Chen, J.; Chabera, P.; Schaller, R.; Al-Marri, M. J.; Canton, S. E.; Liang, Z.; Pullerits, T. Efficient Charge Separation and Exciton Dissociation in Two-Dimensional Ruddlesden-Popper Hybrid Perovskites. *J. Mater. Chem. A* **2018**, *6*, 6244–6250.
- (13) Zhao, Y.-Q.; Ma, Q.-R.; Liu, B.; Yu, Z.-L.; Yang, J.; Cai, M.-Q. Progress in Two-Dimensional Layered Halide Perovskites for Optoelectronic Applications. *Nanoscale* **2018**, *10*, 8677–8688.
- (14) Abid, H.; Hlil, E. K.; Abid, Y. Spectroscopic Ellipsometry thin film and First principles calculations of electronic and linear optical properties of [(C9H19NH3)2PbI2Br2] 2D perovskite. *J. Solid State Chem.* **2017**, *247*, 131–136.
- (15) Li, H.; Wang, X.; Zhang, T.; Gong, X.; Sun, Q.; Pan, H.; Shen, Y.; Ahmad, S.; Wang, M. 2D Ruddlesden-Popper Perovskite with Wide Temperature Window for Stable Solar Cells. *Adv. Funct. Mater.* **2019**, *29*, 1903293.
- (16) Dong, Y.; Lu, D.; Xu, Z.; Lai, H.; Liu, Y. Two-Dimensional Layered Perovskite Materials: From Synthesis to Energy-Related Applications. *Adv. Energy Mater.* **2020**, *10*, 2000694.
- (17) Xi, J.; Spanopoulos, I.; Bang, K.; Xu, J.; Dong, H.; Yang, Y.; Malliakas, C. D.; Hoffman, J. M.; Kanatzidis, M. G.; Wu, Z. Scalable Exfoliation of Layered Halide Perovskites. *J. Am. Chem. Soc.* **2020**, *142*, 19705.
- (18) Li, J.; Yu, Q.; He, Y.; Stoumpos, C. C.; Niu, G.; Trimarchi, G. G.; Guo, H.; Dong, G.; Wang, D.; Wang, L.; Kanatzidis, M. G. Cs<sub>2</sub>PbI<sub>2</sub>Cl<sub>2</sub>, All-Inorganic Two-Dimensional Ruddlesden-Popper Mixed Halide Perovskite with Optoelectronic Response. *J. Am. Chem. Soc.* **2018**, *140*, 11085–11090.
- (19) Pan, L. Y.; Ding, Y. F.; Yu, Z. L.; Wan, Q.; Liu, B.; Cai, M. Q. Hierarchical Mesoporous SnO<sub>2</sub>/Carbon Nanofiber Composite Anodes for High-Performance Lithium-Ion Batteries. *J. Power Sources* **2020**, *451*, No. 227732.
- (20) Xu, Z.; Chen, M.; Liu, S. F. Defect-Induced Modulation of Electronic Properties in Two-Dimensional Materials: A First-Principles Study. *J. Phys. Chem. C* **2019**, *123*, 27978.
- (21) Saffari, M.; Zarei, M.; Tagani, M. B.; Soleimani, H. R. Cs<sub>2</sub>XI<sub>2</sub>Cl<sub>2</sub> (X = Pb, Sn) All-Inorganic Layered Ruddlesden-Popper Mixed Halide Perovskite Single Junction and Tandem Solar Cells: Ultra-High Carrier Mobility and Excellent Power Conversion Efficiency. *Energy Technol.* **2023**, *11*, No. 2201050, DOI: 10.1002/ente.202201050.
- (22) Smidstrup, S.; Markussen, T.; Vancraeyveld, P.; Wellendorff, J.; Schneider, J.; Gunst, T.; Verstichel, B.; Stradi, D.; Khomyakov, P. A.; Vej-Hansen, U. G.; et al. QuantumATK: An Integrated Platform of Electronic and Atomic-Scale Modelling Tools. *J. Phys.: Condens. Matter* **2020**, *32*, No. 015901.
- (23) Perdew, J. P.; Burke, K.; Ernzerhof, M. Generalized Gradient Approximation Made Simple. *Phys. Rev. Lett.* **1996**, *77*, 3865–3868.
- (24) Van Setten, M.; Giantomassi, M.; Bousquet, E.; Verstraete, M.; Hamann, D.; Gonze, X.; Rignanese, G.-M. The PseudoDojo: Training and Grading a 85 Element Optimized Norm-Conserving Pseudopotential Table. *Comput. Phys. Commun.* **2018**, *226*, 39–54.
- (25) Monkhorst, H. J.; Pack, J. D. Special Points for Brillouin-Zone Integrations. *Phys. Rev. B* **1976**, *13*, 5188–5192.
- (26) Grimme, S. Semiempirical GGA-Type Density Functional Constructed with a Long-Range Dispersion Correction. *J. Comput. Chem.* **2006**, *27* (15), 1787–1799.
- (27) Heyd, J.; Scuseria, G. E.; Ernzerhof, M. Hybrid Functionals Based on a Screened Coulomb Potential. *J. Chem. Phys.* **2003**, *118*, 8207–8215.
- (28) Kanoun, M. B.; Goumri-Said, S.; Schwingenschlöggl, U.; Manchon, A. Magnetism in Sc-Doped ZnO with Zinc Vacancies: A Hybrid Density Functional and GGA+U Approaches. *Chem. Phys. Lett.* **2012**, *532*, 96–99.
- (29) Ikram, M.; Haider, A.; Tayaba Bibi, S.; Ul-Hamid, A.; Haider, J.; Shahzadi, I.; Nabgan, W.; Moeen, S.; Ali, S.; Goumri-Said, S.; Kanoun, M. B. Synthesis of Al/Starch Co-Doped in CaO Nanoparticles for Enhanced Catalytic and Antimicrobial Activities: Experimental and DFT Approaches. *RSC Adv.* **2022**, *12*, 32142.
- (30) Ikram, M.; Wakeel, M.; Hassan, J.; Haider, A.; Naz, S.; Ul-Hamid, A.; Haider, J.; Ali, S.; Goumri-Said, S.; Kanoun, M. B. Impact of Bi Doping into Boron Nitride Nanosheets on Electronic and Optical Properties Using Theoretical Calculations and Experiments. *Nanoscale Res. Lett.* **2021**, *16*, 82 DOI: 10.1186/s11671-021-03542-x.
- (31) Stoumpos, C. C.; Cao, D. H.; Clark, D. J.; Young, J.; Rondinelli, J. M.; Jang, J. I.; Hupp, J. T.; Kanatzidis, M. G. Ruddlesden-Popper Hybrid Lead Iodide Perovskite 2D Homologous Semiconductors. *Chem. Mater.* **2016**, *28*, 2852–2867.
- (32) Snaith, H. J. Perovskites: The Emergence of a New Era for Low-Cost, High-Efficiency Solar Cells. *J. Phys. Chem. Lett.* **2013**, *4*, 3623–3630.
- (33) Kanoun-Bouayed, N.; Kanoun, M. B.; Kanoun, A.-A.; Goumri-Said, S. Insights into the Impact of Metal Tin Substitution on Methylammonium Lead Bromide Perovskite Performance for Photovoltaic Application. *Sol. Energy* **2021**, *224*, 76–81.
- (34) Wu, D.; Zhang, X.; Jing, Y.; Zhao, X.; Zhou, Z. High Performance and High-Temperature Stable Planar Perovskite Solar Cells Based on an Ultra-Thin 2D/3D Hybrid Perovskite. *Nano Energy* **2016**, *28*, 390–396.
- (35) Li, J.; Stoumpos, C. C.; Trimarchi, G. G.; Chung, I.; Mao, L.; Chen, M.; Wasielewski, M. R.; Wang, L.; Kanatzidis, M. G. Air-Stable Direct Bandgap Perovskite Semiconductors: All-Inorganic Tin-Based Heteroleptic Halides A<sub>x</sub>SnClyIz (A = Cs, Rb). *Chem. Mater.* **2018**, *30*, 4847–4856.
- (36) Pan, L.-Y.; Ding, Y.-F.; Yu, Z.-L.; Wan, Q.; Liu, B.; Cai, M.-Q. Layer-Dependent Optoelectronic Property for All-Inorganic Two-Dimensional Mixed Halide Perovskite Cs<sub>2</sub>PbI<sub>2</sub>Cl<sub>2</sub> with a Ruddlesden-Popper Structure. *J. Power Sources* **2020**, *451*, No. 227732.
- (37) Xu, Z.; Chen, M.; Liu, S. F. Layer-Dependent Ultrahigh-Mobility Transport Properties in All-Inorganic Two-Dimensional Cs<sub>2</sub>PbI<sub>2</sub>Cl<sub>2</sub> and Cs<sub>2</sub>SnI<sub>2</sub>Cl<sub>2</sub> Perovskites. *J. Phys. Chem. C* **2019**, *123*, 27978–27985.
- (38) Kanoun, M. B.; Goumri-Said, S. Insights into the impact of Mn-doped inorganic CsPbBr<sub>3</sub> perovskite on electronic structures and magnetism for photovoltaic application. *Materials Today Energy* **2021**, *21*, No. 100796.
- (39) Kanoun, M. B.; Goumri-Said, S. Exploring performances of hybrid perovskites tin-based photovoltaic solar cells: Non-equilibrium Green's functions and macroscopic approaches. *Phys. B* **2020**, *591*, No. 412247.
- (40) Slack, G. A. Nonmetallic Crystals with High Thermal Conductivity and Their Thermoelectric Properties. *CRC Crit. Rev. Solid State Mater. Sci.* **1997**, *22* (2), 147–187.
- (41) Mahan, G.; Sofo, J. O. The Best Thermoelectric. *Proc. Natl. Acad. Sci. U. S. A.* **1996**, *93* (15), 7436–7439.
- (42) Singh, D. J. Thermoelectric Materials Theory: Boltzmann Transport. In *Encyclopedia of Materials: Science and Technology*; Elsevier, 2001; pp 9433–9445.
- (43) Goumri-Said, S. Probing Optoelectronic and Thermoelectric Properties of Lead-Free Perovskite SnTiO<sub>3</sub>; HSE06 and Boltzmann Transport Calculations. *Crystals* **2022**, *12*, 1317.
- (44) Azam, S.; Goumri-Said, S.; Khan, S. A.; Ozisik, H.; Deligoz, E.; Kanoun, M. B.; Khan, W. Electronic structure and related optical, thermoelectric and dynamical properties of Lilianite-type Pb<sub>7</sub>Bi<sub>4</sub>Se<sub>13</sub>: Ab-initio and Boltzmann transport theory. *Materialia* **2020**, *10*, No. 100658.
- (45) Azam, S.; Goumri-Said, S.; Khan, S. A.; Kanoun, M. B. Electronic, optical and thermoelectric properties of new metal-rich homological selenides with palladium-indium: Density functional theory and Boltzmann transport model. *J. Phys. Chem. Solids* **2020**, *138*, No. 109229.
- (46) Balandin, A. A.; Ghosh, S.; Bao, W.; et al. Superior thermal conductivity of single-layer graphene. *Nano Lett.* **2008**, *8* (3), 902–907.

- (47) Sevinçli, H.; Brandbyge, M. Thermoelectric properties of defected graphene nanoribbons. *J. Appl. Phys.* **2014**, *115* (12), 124309.
- (48) Sevinçli, H.; Brandbyge, M. Edge-disorder-induced enhancement of thermoelectric properties of graphene nanoribbons. *Phys. Rev. B* **2016**, *94* (7), No. 075417.
- (49) Li, W.; Carrete, J.; Mingo, N. Thermal conductivity and phonon transport in two-dimensional transition metal dichalcogenides. *J. Phys. Chem. Lett.* **2015**, *6* (13), 2605–2610.
- (50) Wu, B. R.; Wang, Z.; Lin, Z. Thermoelectric properties of monolayer MoS<sub>2</sub> with sulfur vacancy defects. *J. Appl. Phys.* **2018**, *123* (16), 164302.
- (51) Kumar, A.; Ouyang, Y. Recent advances in two-dimensional transition metal dichalcogenide-based thermoelectric materials and devices. *Nanotechnology* **2019**, *30* (7), No. 072001.
- (52) Qiu, D. Y.; da Jornada, F. H.; Louie, S. G. Optical spectrum of black phosphorus: An ab initio study. *Phys. Rev. Lett.* **2015**, *115* (17), No. 176801.
- (53) Fei, R.; Yang, L. Strain-engineering the anisotropic electrical conductance of black phosphorus. *Nano Lett.* **2016**, *16* (12), 7274–7280.
- (54) Zhu, H.; Wang, J.; Xiao, J.; et al. Achieving high power factor and output power density in *p*-type black phosphorus by electrochemical doping. *Nat. Commun.* **2016**, *7*, 11205.